








RESEARCH ARTICLE OPEN ACCESS

Chemical and Electronic Structure of the $i\text{-ZnO}/\text{In}_x\text{S}_y\text{:Na}$ Front Contact Interface in $\text{Cu}(\text{In,Ga})(\text{S,Se})_2$ Thin-Film Solar Cells

Dirk Hauschild^{1,2,3}  | Frank Meyer^{4,5} | Andreas Benkert^{1,4} | Thomas Dalibor⁶  | Monika Blum^{7,8}  | Wanli Yang⁷  | Friedrich Reinert⁴  | Clemens Heske^{1,2,3}  | Lothar Weinhardt^{1,2,3} 

¹Institute for Photon Science and Synchrotron Radiation (IPS), Karlsruhe Institute of Technology (KIT), Karlsruhe, Germany | ²Institute for Chemical Technology and Polymer Chemistry (ITCP), Karlsruhe Institute of Technology (KIT), Karlsruhe, Germany | ³Department of Chemistry and Biochemistry, University of Nevada, Las Vegas (UNLV), Las Vegas, Nevada, USA | ⁴Experimental Physics VII, University of Würzburg, Würzburg, Germany | ⁵Fraunhofer-Institut für Werkstoffmechanik IWM Freiburg, Freiburg, Germany | ⁶AVANCIS GmbH Munich, Munich, Germany | ⁷Advanced Light Source (ALS), Lawrence Berkeley National Laboratory, Berkeley, California, USA | ⁸Chemical Sciences Division, Lawrence Berkeley National Laboratory, Berkeley, California, USA

Correspondence: Dirk Hauschild (dirk.hauschild@kit.edu) | Lothar Weinhardt (lothar.weinhardt@kit.edu)

Received: 10 April 2024 | **Revised:** 1 July 2024 | **Accepted:** 17 July 2024

Funding: D.H., C.H., and L.W. received funding from the German Federal Ministry for Economic Affairs and Climate Action (BMWK) for the projects “EFFCIS-I” (Nos. 0324076E and 0324076G) and “EFFCIS-II” (No. 03EE1059E).

Keywords: chalcopyrite | chemical structure | electron spectroscopy | electronic structure | front contact | indium sulfide | interface | IPES | $i\text{-ZnO}$ | thin-film solar cell | UPS | XES | XPS | x-ray spectroscopy

ABSTRACT

The chemical and electronic structure of the front contact $i\text{-ZnO}/\text{In}_x\text{S}_y\text{:Na}$ interface for $\text{Cu}(\text{In,Ga})(\text{S,Se})_2$ -based thin-film solar cells is investigated using a combination of x-ray and electron spectroscopies. Upon $i\text{-ZnO}$ sputter deposition on the $\text{In}_x\text{S}_y\text{:Na}$ buffer layer, we find an intermixed heterojunction and the formation of InO_x and Na_2SO_4 . The window layer is shown to consist of a mixture of $\text{Zn}(\text{OH})_2$ and ZnO , with decreasing relative $\text{Zn}(\text{OH})_2$ content for thicker window layers. Moreover, we observe diffusion of sodium to the surface of the window layer. We derive electronic surface band gaps of the $i\text{-ZnO}$ and $\text{In}_x\text{S}_y\text{:Na}$ layers of 3.86 ± 0.18 eV and 2.60 ± 0.18 eV, respectively, and find a largely flat conduction band alignment at the $i\text{-ZnO}/\text{In}_x\text{S}_y\text{:Na}$ interface.

1 | Introduction

$\text{Cu}(\text{In,Ga})(\text{S,Se})_2$ (CIGSSe)-based solar cells consist of a multi-layer structure—from top to bottom: $n\text{-ZnO:Al}/i\text{-ZnO}/\text{buffer layer}/\text{CIGSSe}/\text{Mo}/\text{glass substrate}$. Traditionally, CdS, prepared via chemical bath deposition (CBD), is the most common buffer layer material. To decrease absorption in the buffer layer and reduce the amount of waste from the CBD-CdS process, intensive research efforts have focused on alternative buffer layer materials, deposited in a dry process compatible with industrial in-line production [1, 2]. Several buffer layer candidates, for example, $\text{Zn}(\text{O,S})$ [3], $(\text{Zn,Mg})\text{O}$ [4], and In_2S_3 [5, 6], were proposed

and, in some cases, have successfully replaced CdS in the solar cell production process. Among these buffer layer candidates, Avancis has successfully optimized sodium-doped indium sulfide ($\text{In}_x\text{S}_y\text{:Na}$) buffer layers with corresponding thin-film solar cell mini-modules ($30 \times 30 \text{ cm}^2$), showing certified efficiencies of 17.9% [7].

The efficiency of thin-film solar cells, in general, crucially depends on the properties at the various interfaces within the multilayer structure. When replacing one (or several) of these layers, it is thus very important to reoptimize and characterize the modified interfaces. When replacing the CdS buffer by $\text{In}_x\text{S}_y\text{:Na}$,

This is an open access article under the terms of the [Creative Commons Attribution-NonCommercial-NoDerivs](https://creativecommons.org/licenses/by-nc-nd/4.0/) License, which permits use and distribution in any medium, provided the original work is properly cited, the use is non-commercial and no modifications or adaptations are made.

© 2024 The Author(s). *Progress in Photovoltaics: Research and Applications* published by John Wiley & Sons Ltd.

two interfaces are directly affected: the buffer/CIGSSe interface and the i-ZnO/buffer interface. In earlier work, we have investigated In_xS_y and $\text{In}_x\text{S}_y\text{:Na}$ buffer layers and their interface with the CIGSSe absorber [8, 9]. We found a diffusion of copper into the In_xS_y buffer [8], the magnitude of which is reduced when using a sodium-doped buffer layer [9]. Additionally, we found a diffusion of Se into the sodium-doped buffer layer upon annealing to temperatures similar to those employed in the window layer deposition process.

In contrast to the buffer/absorber interface, the i-ZnO/buffer layer interface is less frequently investigated. In the case of an indium sulfide buffer layer, it was found that the i-ZnO thickness and the oxygen content during the sputter process influence the overall device performance [10]. Nguyen et al. found acceptor-like defect states for a CBD- $\text{In}(\text{OH}_x\text{S}_y)$ buffer layer at the i-ZnO/ $\text{In}(\text{OH}_x\text{S}_y)$ interface, leading to a reduced solar cell performance [11]. Furthermore, it was suggested that a post-annealing step alters the acceptor-like defects [12].

For the i-ZnO layer/CdS interface, the beneficial effect of the i-ZnO layer is reflected in an improvement of the fill factor as well as the open-circuit voltage [13–16]. It was suggested that the i-ZnO layer reduces electrical shunt paths caused by “bad” CIGSSe crystallites [13, 17]. A direct measurement of the band alignment revealed a flat conduction band alignment at the i-ZnO layer/CdS interface [18]. It was also reported that CdSO_4 is formed during i-ZnO deposition [19], whereas others found no intermixing at the i-ZnO/CdS interface and even a removal of sulfate, formerly present at the CdS surface, during the i-ZnO sputter deposition [18, 20].

In this paper, we present a detailed investigation of the chemical and electronic structure of the i-ZnO/ $\text{In}_x\text{S}_y\text{:Na}$ interface. For this purpose, we have employed surface-sensitive x-ray photoelectron spectroscopy (XPS), x-ray-excited Auger electron spectroscopy (XAES), and bulk-sensitive soft x-ray emission spectroscopy (XES) to reveal a depth-varied picture of the chemical structure of the i-ZnO/ $\text{In}_x\text{S}_y\text{:Na}$ interface. Using ultraviolet photoelectron spectroscopy (UPS) and inverse photoemission spectroscopy (IPES), we determine the band edge positions and their alignment at the i-ZnO/ $\text{In}_x\text{S}_y\text{:Na}$ interface.

2 | Experimental Section

The samples were processed as described in [9] (and references therein). Briefly, CIGSSe absorbers were grown using the Avancis pilot line in Munich, Germany. An $\text{In}_x\text{S}_y\text{:Na}$ buffer layer with a nominal thickness of 48 nm was deposited onto CIGSSe with a physical vapor deposition (PVD). Subsequently, i-ZnO layers were radio-frequency (RF) sputtered with different thicknesses (1, 3, 5, 10, 50, and 100 nm). At Avancis, the sample series was sealed under a dry nitrogen atmosphere to minimize the possible influence of adsorbates due to the ambient environment, shipped to the University of Würzburg, and subsequently transferred into the ultra-high vacuum chamber (base pressure $< 2 \times 10^{-10}$ mbar). At the University of Würzburg, the air exposure was limited to less than 1 min. The surface-sensitive measurements were performed with a VG CLAM 4 electron analyzer, a non-monochromatized Mg and Al K_α twin-anode x-ray source

(XPS), and a He discharge lamp (UPS). To reduce unwanted surface adsorbates, the samples were treated with low-energy Ar^+ ions (50 eV, $j_{\text{sample}} \sim 50 \text{ nA/cm}^2$) using a VG EX05 ion source. IPES was performed with a STAIB NEK-150-1 electron gun and a custom-made photon detector using a Hamamatsu photomultiplier (PMP) tube C 9744 and a Semrock Hg01-254 band pass with a central photon energy of 4.88 eV. Sputter-cleaned Au, Ag, and Cu foils were used to calibrate the electron spectrometer [21]. The Au and Cu foils were also used for the energy calibration of the Fermi edge in UPS and IPES, respectively.

After the surface-sensitive dataset was taken, the samples were sealed under dry nitrogen atmosphere and shipped to Beamline 8.0.1 at the Advanced Light Source (ALS), Lawrence Berkeley National Laboratory, for soft XES. The S $L_{2,3}$ emission spectra were measured using the SALSA endstation [22] with its high-transmission soft x-ray spectrometer [23]. The emission energy axis was calibrated using characteristic features of BN and CaSO_4 [24].

3 | Results and Discussion

3.1 | Chemical Structure

Selected i-ZnO/ $\text{In}_x\text{S}_y\text{:Na}$ XPS survey spectra are depicted in Figure 1. With increasing i-ZnO thickness, the lines of the buffer layer elements (i.e., indium and sulfur) are attenuated and not visible anymore for the 10 nm i-ZnO sample, suggesting a closed i-ZnO layer. In parallel, the intensities of the zinc- and oxygen-related peaks increase, as expected. For thicknesses larger than 10 nm, the survey spectra of the i-ZnO layers are almost identical. The Na 1s line intensity increases for increasing i-ZnO thickness and reaches a maximum for the 10 nm sample ($\times 2.5$ of the $\text{In}_x\text{S}_y\text{:Na}$ surface value). Subsequently, it decreases by $\sim 25\%$ for the 100 nm i-ZnO sample. As all other absorber-related peaks are fully attenuated for ≥ 10 nm i-ZnO thickness, this result suggests

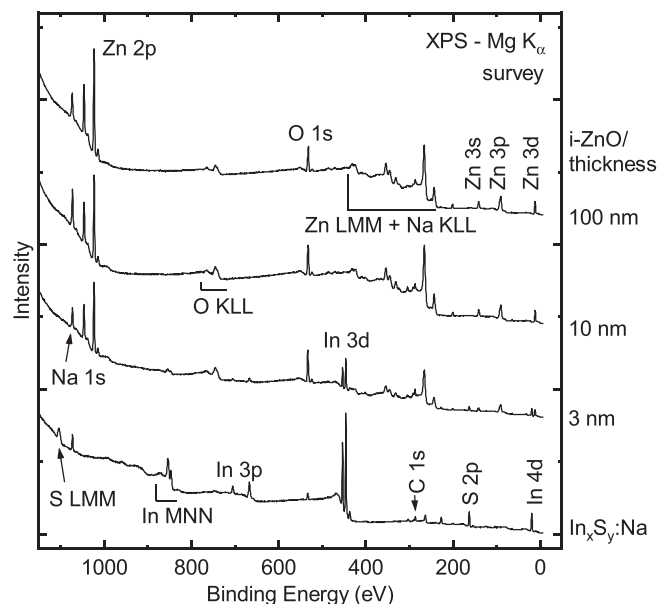


FIGURE 1 | Mg K_α excited XPS survey spectra of the as-received $\text{In}_x\text{S}_y\text{:Na}$ buffer layer surface and the 3, 10, and 100 nm i-ZnO/ $\text{In}_x\text{S}_y\text{:Na}$ samples. Prominent photoelectron and Auger signals are labeled.

that the i-ZnO layer is closed and that sodium diffuses from the buffer layer to the i-ZnO surface during the sputter deposition process or during subsequent sample handling. It is well known that sodium accumulates at surfaces of chalcopyrite absorbers [25–29], and a diffusion of sodium towards the ZnO surface was observed by Erfurth et al. [30] The elevated temperatures during the sputtering processes may also lead to an enhanced diffusion of sodium [25].

To study the interface formation in more detail, we investigate the In MNN Auger and S 2p XPS lines for i-ZnO/ In_xS_y :Na samples up to a thickness of 10 nm, as shown in Figure 2 (left). The In MNN signal of the buffer layer surface resembles the spectral signature typically found for indium in a single sulfide environment [29, 32, 33]. With increasing window layer thickness, the In MNN signal decreases (as expected) and fully vanishes for the 10 nm sample. Furthermore, the In MNN emission shifts to lower kinetic energies, and the spectral features broaden. This indicates both a change of the chemical environment and an emergence of additional chemical environments. To analyze the change in the spectral signature, we fitted the spectra of the 1, 3, and 5 nm i-ZnO/ In_xS_y :Na samples with several species, each represented by the line profile (spectrum) of the buffer layer and shifted along the energy axis. However, the fit with up to four such species (with a total of eight fit parameters) did not give a satisfactory description of the spectra. In contrast, a fit with only *one* buffer layer spectrum but with an additional convolution (broadening) with a Gaussian gives an excellent description of the data (see red lines for the 1, 3, and 5 nm samples). Note that this approach only requires three fit parameters: relative energy shift, intensity, and Gaussian width.

In the fits, the derived energy shift for the 1 and 3 nm samples is $0.69 (\pm 0.02)$ eV and $0.60 (\pm 0.02)$ eV for the 5 nm sample. These shifts indicate a transition from an indium sulfide towards an indium *oxide* chemical environment. For all three samples, the fit-derived full width at half maximum (FWHM)

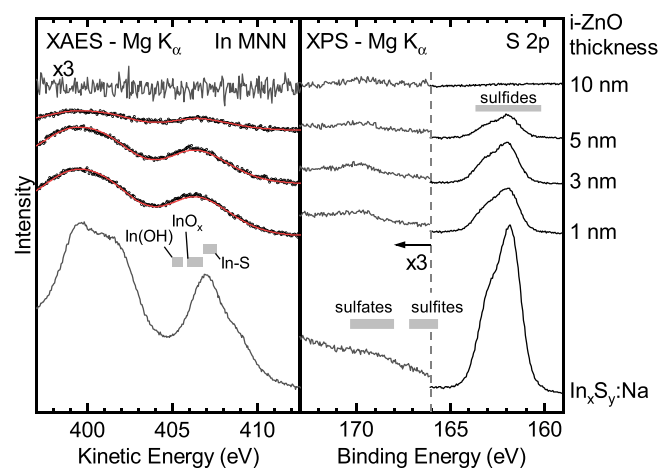


FIGURE 2 | Mg K_{α} excited In MNN XAES (left) and S 2p XPS (right) spectra for increasing i-ZnO window layer thickness. The In MNN spectra of the 1, 3, and 5 nm i-ZnO/ In_xS_y :Na samples were fitted (red line) as described in the text. The In MNN spectrum of the 10 nm i-ZnO sample and the S 2p binding energy region above 166 eV are magnified by a factor of 3. The gray bars mark energy ranges commonly found for the most prominent and relevant chemical environments [21, 31].

of the Gaussian broadening is $2.3 (\pm 0.1)$ eV. We interpret the significant broadening with the presence of a broad distribution of different In-O environments. Some remaining contributions from In-S environments are also likely (and apparently sufficiently well described by the Gaussian broadening of one chemical species).

The S 2p component in Figure 2 (right) at ~ 162 eV can be directly assigned to a sulfidic environment, that is, indium sulfide (In_xS_y). Its intensity decreases with increasing i-ZnO thickness, in accordance with the nominal window layer thickness. Moreover, a second (weak) S component can be observed at $E_{\text{bind}} \sim 169$ eV for all samples with ≤ 10 nm i-ZnO; this component can be attributed to oxidized sulfur species, most likely a sulfate (SO_4^{2-}). Although, for the buffer layer surface, the sulfate-related signal is very small, its intensity relative to the sulfide peak increases with increasing window layer thickness. For the 1–5 nm i-ZnO samples, $\sim 5\%$ of the (overall decreasing) sulfur signal stems from sulfur in a sulfate environment; the 10 nm i-ZnO/ In_xS_y :Na sample exhibits only a (very weak) sulfate peak. This indicates that the i-ZnO sputter process breaks some of the sulfide bonds, S–O bonds are formed, and intermixing at the i-ZnO window layer/buffer layer interface occurs. This will be further discussed in conjunction with Figure 4.

To study the chemical environment of zinc, the Zn $2p_{3/2}$ and Zn $L_3M_{45}M_{45}$ spectra are plotted as a function of increasing i-ZnO layer thickness in Figure 3 (left). For the Zn $2p_{3/2}$ peak, an intensity increase (as expected) and a shift to lower binding energies (by ~ 0.5 eV) can be observed for increasing i-ZnO thickness. All peak positions are in good agreement with literature values commonly found for ZnO [21, 31, 34].

The Zn LMM Auger signal overlaps energetically with the Na KLL Auger signal. This can be best seen for the In_xS_y :Na buffer layer sample in Figure 3 (left), for which no Zn-related signals are observed. The Na KLL maximum at 991.4 eV is marked with a gray dashed line throughout the series. At this energy, all i-ZnO samples exhibit a shoulder, which is partly due to the Na KLL emission but also due to Zn $L_3M_5M_5$ transitions appearing at the same energy. We find that the spectral shape of the Zn LMM changes significantly with increasing i-ZnO thickness. The 1 and 3 nm samples exhibit a shoulder at ~ 986.5 eV, which decreases for the 5 nm sample, whereas the 10–100 nm samples show Zn LMM signals similar to those reported for ZnO [30, 35–38]. The shoulder for the 1–5 nm i-ZnO samples indicates (at least) one additional chemical environment of Zn (e.g., $\text{Zn}(\text{OH})_2$; see discussion below).

For further insights, the modified Zn Auger parameter α'_{Zn} is calculated by adding the Zn $2p_{3/2}$ binding energy and the kinetic energy of the Zn $L_3M_{45}M_{45}$ maximum [39]. For the 1–5 nm i-ZnO samples, the complex spectral structure of the Zn LMM emission and the overlap with the Na KLL Auger (which possibly also shifts due to a changing chemical environment) make it difficult to determine the maximum, and hence, we refrain from calculating α'_{Zn} for these samples. For the 10 and 50 nm i-ZnO samples, we find an α'_{Zn} of 2010.72 ± 0.10 eV, which further decreases to 2010.43 ± 0.08 eV for the 100 nm sample. This suggests the formation of Zn-O bonds ($2010.3 \leq \alpha'_{\text{ZnO}} \leq 2011.0$ eV), as expected [21, 31].

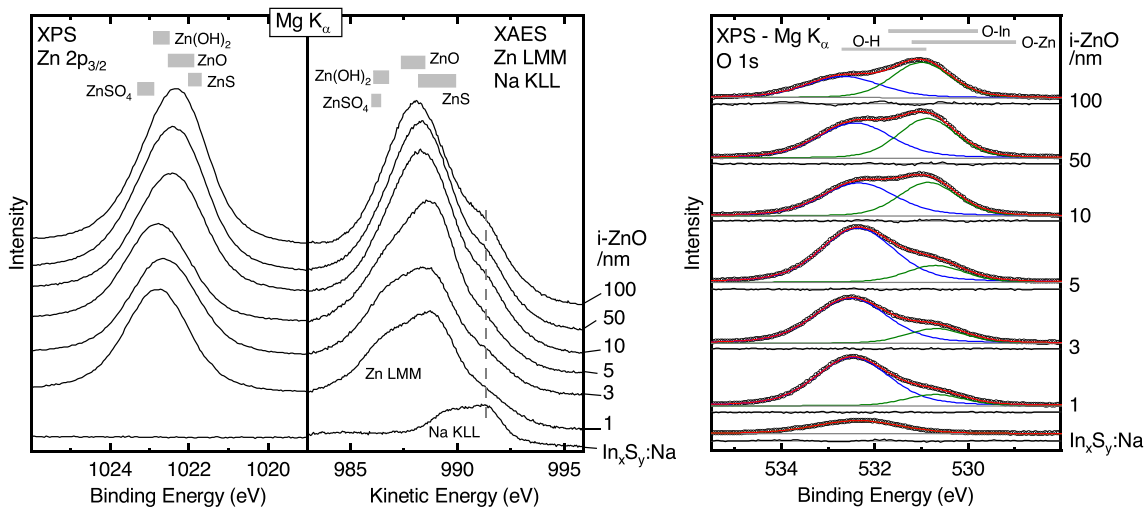


FIGURE 3 | (Left) Mg K_{α} excited Zn $2p_{3/2}$ XPS and Zn $L_{3}M_{4,5}M_{4,5}$ XAES spectra for increasing i-ZnO layer thickness. The gray bars mark energy ranges commonly found for Zn(OH)₂, ZnO, ZnS, and Zn(SO₄) [21, 31, 34]. (Right) Mg K_{α} O 1s XPS spectra for increasing i-ZnO layer thickness. The fit (red) shows the O–H (blue) and O–Zn/O–In (green) component. The magnified fit residuals ($\times 2$) are shown below the respective spectra.

The O 1s peak is investigated (Figure 3, right) to study the local chemical environment of oxygen. The $\text{In}_x\text{S}_y:\text{Na}$ sample exhibits oxygen-containing surface adsorbates, indicated by the nonzero O 1s signal. For all i-ZnO samples, the O 1s signal is significantly increased (as expected) and consists of two overlapping peaks. For the “thin” (1, 3, and 5 nm) i-ZnO samples, the main peak is found at a binding energy of ~ 532.5 eV, with a second component at lower binding energies of ~ 530.5 eV. We assign the high- and low-binding energy contributions to hydroxide (e.g., Zn(OH)₂) and oxide (e.g., ZnO), respectively [31, 40–42]. In contrast, the balance is reversed for the 10, 50, and 100 nm i-ZnO samples: The oxide peak is more intense than the hydroxide peak. To quantify this change, a simultaneous fit of the O 1s region with two Voigt profiles with equal widths and shapes and a linear background was performed. Using the area under the Voigt profiles, the $\text{ZnO}/[\text{ZnO} + \text{Zn(OH)}_2]$ ratio can be computed using $\text{O } 1s(\text{O–Zn})/[\text{O } 1s(\text{O–Zn}) + \frac{1}{2} \text{O } 1s(\text{O–H})]$. Note that small contributions of different In–O environments might influence the determination of the ratio for the thinnest i-ZnO samples. For the 1 nm i-ZnO sample, we find a $\text{ZnO}/[\text{ZnO} + \text{Zn(OH)}_2]$ ratio of 25%, which increases to 31% (3 and 5 nm), 60% (10 and 50 nm), and 71% for the 100 nm i-ZnO sample. This finding is in line with the spectral changes found for the Zn LMM Auger emission in Figure 3 (left). Hydroxides are often present in ZnO thin films and can partly be removed by Ar^+ -ion treatments, by prolonged x-ray exposure, by vacuum, and by elevated temperatures [18, 40, 42, 43]. In the present case, the samples were not treated by Ar^+ ions, and each sample was exposed to x-rays for a similar time at the same temperature, suggesting that these parameters are not responsible for the observed variation in relative hydroxide content. Rather, it is most likely that the reduced hydroxide fraction in the thicker layers is caused by the manufacturing process, for example, due to increased temperatures for longer processing times.

To further investigate the chemical environment of the i-ZnO/ $\text{In}_x\text{S}_y:\text{Na}$ interface, the increased attenuation length of soft x-rays (as compared to electrons) is employed. In Figure 4 (top), the upper valence band region in the $S L_{2,3}$ XES spectra of the 3 nm i-ZnO/ $\text{In}_x\text{S}_y:\text{Na}$ [(a), red solid] and $\text{In}_x\text{S}_y:\text{Na}$ [(b), red dashed]

spectra is presented, together with the difference “3 nm i-ZnO/ $\text{In}_x\text{S}_y:\text{Na}$ – $0.97 \times \text{In}_x\text{S}_y:\text{Na}$ ” (blue) and four references (black).

The spectrum of the $\text{In}_x\text{S}_y:\text{Na}$ buffer layer (b) resembles the characteristic $\text{In}_2\text{S}_3 S L_{2,3}$ spectral signature [8, 9, 44]. The spectrum of the 3 nm i-ZnO/ $\text{In}_x\text{S}_y:\text{Na}$ sample is similar to that of $\text{In}_x\text{S}_y:\text{Na}$, but two additional sharp features at ~ 155 and ~ 156.5 eV (marked (2)) and a broad feature at ~ 162 eV (marked (3)) appear (whereas the absence of the S–Zn-related features marked (1) excludes a substantial presence of S–Zn bonds at this interface). Signals (2) and (3) indicate the formation of sulfate [24, 45, 46] (consistent with the XPS findings). The former two features can be assigned to transitions from the “S 3s-related” states to S 2p core holes (with a binding energy relating to a sulfate). The latter signal stems from “S 3d-related” states, which become occupied in sulfates [24, 47]. To visualize the sulfate chemical environment, the spectrum of $\text{In}_x\text{S}_y:\text{Na}$ (scaled with a factor of 0.97) is subtracted from that of the 3 nm i-ZnO/ $\text{In}_x\text{S}_y:\text{Na}$ sample. The resulting difference spectrum is shown in blue, magnified by a factor of 2, and clearly resembles the spectral signature of the sulfate references shown underneath.

Recently, we were able to show and, in detail, analyze the fact that different sulfates show distinct spectral characteristics even in the $S L_{2,3}$ XES spectra [24]. For a precise sulfate speciation, we have fitted the “S 3s” \rightarrow S $2p_{3/2}$ signal of the blue difference spectrum with a Voigt function and plot the line width and energy ($\text{FWHM} = 0.42 \pm 0.01$ eV and $E_{\text{“S } 3s” \rightarrow \text{S } 2p_{3/2}} = 155.30 \pm 0.02$ eV) in Figure 4 (bottom). This figure shows the FWHM of the “S 3s” \rightarrow S $2p_{3/2}$ transition as a function of the corresponding emission energy for a large number of sulfates [24]. The comparison of the here-obtained datapoint (blue star) with the three possible candidates (Na_2SO_4 , ZnSO_4 , and $\text{In}_2(\text{SO}_4)_3$) identifies the formation of Na_2SO_4 at the i-ZnO/ $\text{In}_x\text{S}_y:\text{Na}$ interface. We speculate that the small deviations (~ 0.1 eV) are due to the different photon excitation energy used in this study ($h\nu_{\text{exc}} = 180$ eV) as compared to [24] ($h\nu_{\text{exc}} = 200$ eV).

To summarize this section on the chemical structure of the i-ZnO/ $\text{In}_x\text{S}_y:\text{Na}$ interface, we find a heterojunction with complex

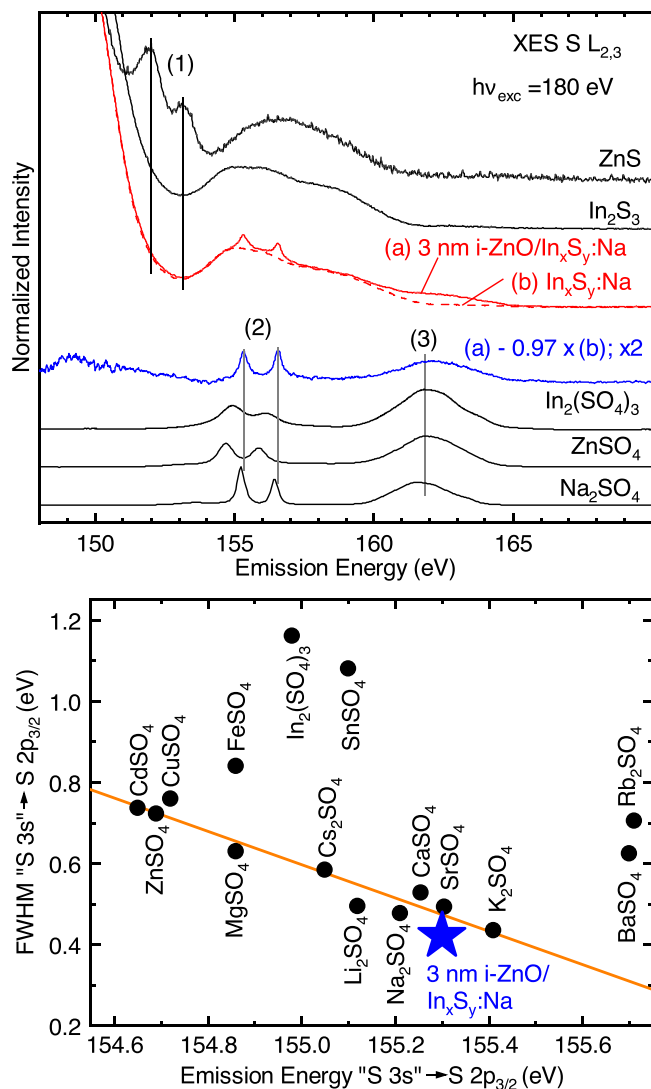


FIGURE 4 | (Top) S L_{2,3} XES spectra (hν_{exc} = 180 eV) of the upper valence band region of 3 nm i-ZnO/In_xS_y:Na (a, red solid), In_xS_y:Na (b, red dashed), the difference "3 nm i-ZnO/In_xS_y:Na" - "0.97 × In_xS_y:Na" (blue), and several references (black) are shown. Features marked (1), (2), and (3) indicate specific chemical environments and are discussed in the text. (Bottom) FWHM of the "S 3s" → S 2p_{3/2} transitions as a function of the corresponding emission energy of various sulfates (from [23]). The orange line serves as a guide to the eye to illustrate the linear dependency. The blue star marks the data point of the 3 nm i-ZnO/In_xS_y:Na sample.

properties. The analysis indicates that the buffer layer is strongly impacted by the i-ZnO sputter deposition. In detail, the formation of a "poorly defined" In-O_x environment, the diffusion of S into the window layer, and the formation of sodium sulfate is identified. We observe diffusion of Na to the surface of the window layer, which contains both ZnO and Zn(OH)₂ with an increasing ZnO/[ZnO + Zn(OH)₂] ratio for increasing window layer thickness.

3.2 | Electronic Structure

The electronic structure at the window/buffer interface plays an important role for the electron transport to the front contact.

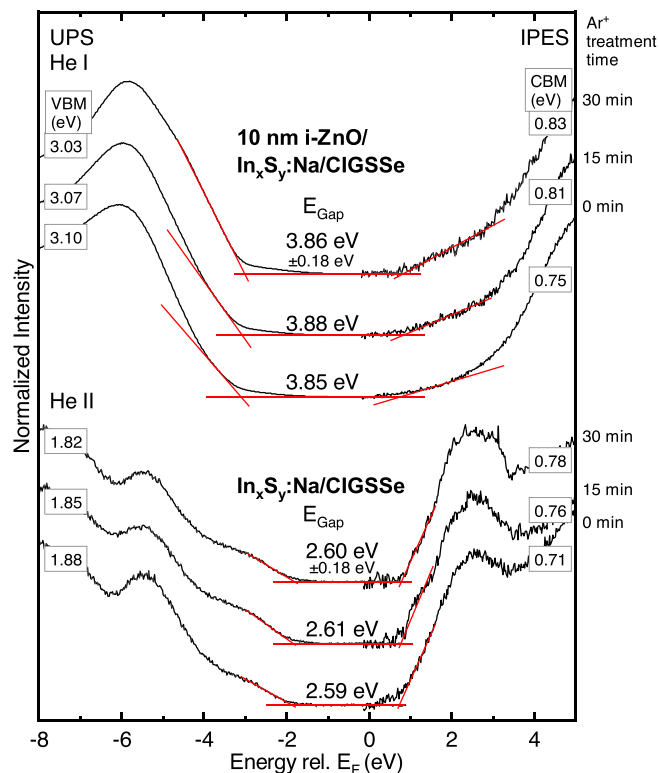


FIGURE 5 | UPS (left) and IPES (right) spectra of the In_xS_y:Na/CIGSse and the 10 nm i-ZnO/In_xS_y:Na/CIGSse samples. Each sample was subjected to a 50 eV Ar⁺-ion treatment with two intervals of 15 min each. The valence band maximum (VBM) and conduction band minimum (CBM) are determined by a linear extrapolation of the leading edges in the spectra and listed in boxes on the left (VBM) and right (CBM) of the respective spectra. The resulting band gaps E_{Gap} are given in the center.

In the following, the valence and conduction band alignment at the i-ZnO/In_xS_y:Na interface are directly and separately derived using a combination of UPS and IPES [48]. Because UPS and IPES are surface-sensitive measurement methods, the samples were cleaned with a low-energy (50 eV) Ar⁺-ion treatment (up to 30 min) and monitored with XPS.

Figure 5 shows the UPS/IPES spectra of the In_xS_y:Na and i-ZnO/In_xS_y:Na samples for different Ar⁺-ion treatment times. The UPS/IPES spectra of the In_xS_y:Na buffer layer and its interface with the CIGSse absorber are already published elsewhere [9]. The linear extrapolations of the leading band edges are used to determine the conduction band minimum (CBM) and valence band maximum (VBM) [49, 50]. The band extrema of the In_xS_y:Na sample do not change significantly after each Ar⁺ treatment step, indicating only a small influence by surface adsorbates. After 30 min of ion treatment, we obtain a VBM of 1.82 ± 0.10 eV and a CBM of 0.78 ± 0.15 eV, leading to an electronic surface band gap of 2.60 ± 0.18 eV.

To determine the band edges of the window layer, the 10 nm i-ZnO sample was used to avoid potential charging effects due to poor conductivity of the thicker i-ZnO layers. As we have shown above, the 10 nm i-ZnO film already represents a closed layer, which justifies this approach. Although He II excitation was used for the UPS measurements of the In_xS_y:Na sample,

the i-ZnO samples were excited with He I to avoid overlap of the VBM with satellite lines of the Zn 3d-derived bands (excited with a He II satellite). For the “as-received” 10 nm i-ZnO, the valence and conduction band edges appear “round”, that is, without a clear linear edge, which we attribute to spectral contributions from surface adsorbates. After treatment with 50 eV Ar⁺ ions, a more pronounced structure appears for both band edges, facilitating a linear extrapolation and demonstrating the importance of nondestructive adsorbate removal. We determine a VBM of 3.03 ± 0.10 eV and a CBM of 0.83 ± 0.15 eV, leading to an electronic surface band gap of 3.86 ± 0.18 eV. The band gap value is larger than reported optical bulk band gaps of 3.3–3.4 eV [51, 52]. In two earlier UPS/IPES measurements, we observed a slightly smaller ($E_{\text{gap}}^{\text{surf}} = 3.52 \text{ eV} \pm 0.15 \text{ eV}$) [18] and a similar surface band gap ($E_{\text{gap}}^{\text{surf}} = 3.8 \pm 0.2 \text{ eV}$) [53], also on samples from Avancis. The surface band gap found in this paper might be further increased by the rather high Zn(OH)₂ content, which has a reported band gap above 5 eV [54]. This is corroborated by the fact that the i-ZnO surface reported in [20] showed a significantly smaller Zn(OH)₂ content. Moreover, additional intensity (a “foot”) is found in the UPS spectrum at about –3 eV, which is not described by the linear extrapolation. Such states have been related to defect states [18], for example, oxygen vacancies, and have been interpreted to be relevant for the charge transport properties [55].

A direct comparison of the CBM values for the In_xS_y:Na and i-ZnO/In_xS_y:Na samples suggests the presence of a flat or slightly positive conduction band offset (of 0.05 ± 0.10 eV). Note that whereas the uncertainty of the absolute CBM is about ± 0.15 eV, the *relative* uncertainty between two CBM measurements is significantly smaller. In a further refinement step, the band extrema need to be corrected for the interface-induced band bending (iibb). In order to track the relative shifts, the buffer and window core levels (i.e., S 2p and In 3d, as well as Zn 2p and the metal oxide component of the O 1s, respectively) were analyzed for the three thin samples (1, 3, and 5 nm i-ZnO thickness) of our series.

While the S 2p core level shows a downward shift (-0.16 ± 0.02 eV), the In 3d core levels shift upwards (0.10 ± 0.03 eV) with increasing i-ZnO thickness. Similarly, the ZnO component of the O 1s signal displays an upward (0.15 ± 0.03 eV) shift, and a downward shift (-0.30 ± 0.06 eV) of the Zn 2p core level is detected. Simply averaging these values, an iibb correction of (-0.04 ± 0.35) eV is calculated. However, the significant variations of these shifts need to be discussed in view of the observed intermixing at the i-ZnO/In_xS_y:Na interface and the associated chemical shifts. We argue that the observed variations are primarily due to the intermixing-induced changes in local chemical structure and exceed the “true” iibb by far. In particular, the assumption of an abrupt non-intermixed interface cannot be upheld for the i-ZnO/In_xS_y:Na interface. Correspondingly, no band bending corrections were applied in the band alignment shown in Figure 6, but the interface is sketched as non-abrupt (as indicated by the encircled red dashed lines). Overall, we depict a “largely flat” (i.e., within the confidence window) conduction band offset of $+0.05$ (± 0.10) and a valence band offset of -1.21 (± 0.08) eV, respectively. Such band alignments allow for an unimpeded electron flow from the buffer to the window layer, although they block the hole transport in the reverse direction; this is in line with the reported high device efficiencies.

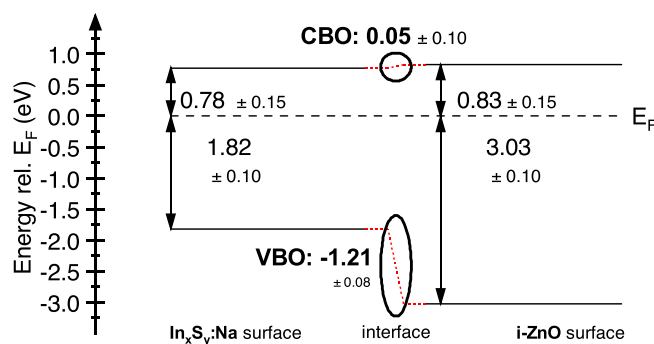


FIGURE 6 | Schematic drawing of the band alignment at the i-ZnO/In_xS_y:Na front contact interface (all values in eV). The determined VBM and CBM of the In_xS_y:Na and i-ZnO surfaces are shown on the left and right, respectively.

4 | Summary

We have studied the chemical and electronic structure of the i-ZnO/In_xS_y:Na interface with surface sensitive photoelectron spectroscopy and bulk-sensitive XES. We find that the i-ZnO sputter deposition creates a complex heterojunction, including the formation of InO_x and Na₂SO₄. The thin i-ZnO window layers consist of a mixture of hydroxide Zn(OH)₂ and ZnO. With increasing i-ZnO thickness, the ZnO/[ZnO + Zn(OH)₂] ratio increases. For this mixed Zn(OH)₂-ZnO layer, we find a surface band gap of 3.72 ± 0.18 eV and a largely flat conduction band alignment at the i-ZnO/In_xS_y:Na interface (0.05 ± 0.10 eV).

Acknowledgments

D.H., C.H., and L.W. thank the German Federal Ministry for Economic Affairs and Climate Action (BMWK) for funding of the projects “EFFCIS-I” (No. 0324076E and 0324076G) and “EFFCIS-II” (No. 03EE1059E). This research used resources of the Advanced Light Source, which is a US Department of Energy (DOE) Office of Science User Facility under Contract No. DE-AC02-05CH11231. We thank Dr. S. Pohlner for fruitful discussions. Open Access funding enabled and organized by Projekt DEAL.

Conflicts of Interest

The authors declare no conflicts of interest.

Data Availability Statement

The data that support the findings of this study are available from the corresponding authors upon reasonable request.

References

1. D. Hariskos, S. Spiering, and M. Powalla, “Buffer Layers in Cu (In,Ga)Se₂ Solar Cells and Modules,” *Thin Solid Films* 480–481 (2005): 99–109, <https://doi.org/10.1016/j.tsf.2004.11.118>.
2. S. Siebentritt, “Alternative Buffers for Chalcopyrite Solar Cells,” *Solar Energy* 77, no. 6 (2004): 767–775, <https://doi.org/10.1016/j.solener.2004.06.018>.
3. M. Nakamura, K. Yamaguchi, Y. Kimoto, Y. Yasaki, T. Kato, and H. Sugimoto, “Cd-Free Cu(In,Ga)(Se,S)₂ Thin-Film Solar Cell With Record Efficiency of 23.35%,” *IEEE Journal of Photovoltaics* 9, no. 6 (2019): 1863–1867, <https://doi.org/10.1109/JPHOTOV.2019.2937218>.

4. C. Platzer-Björkman, T. Törndahl, A. Hultqvist, J. Kessler, and M. Edoff, "Optimization of ALD-(Zn,Mg)O Buffer Layers and (Zn,Mg)O/Cu(In,Ga)Se₂ Interfaces for Thin Film Solar Cells," *Thin Solid Films* 515, no. 15 (2007): 6024–6027, <https://doi.org/10.1016/j.tsf.2006.12.047>.
5. J. Palm, T. Dalibor, R. Lechner, et al., "Cd-Free CIS Thin Film Solar Modules at 17% Efficiency," in *29th European Photovoltaic Solar Energy Conference and Exhibition* (2014), 1433–1438. <https://doi.org/10.4229/EUPVSEC20142014-3AO.4.5>.
6. E. Ghorbani, X. Jin, D. Perera, et al., "Influence of Oxygen Content on the Properties of In₂(O_xS_{1-x})₃ Used as Buffer Material in Cu(In,Ga)Se₂ Solar Cells," *Journal of Applied Physics* 135, no. 7 (2024): 073101, <https://doi.org/10.1063/5.0184698>.
7. "Module With Record Efficiency From AVANCIS: Fraunhofer ISE Certifies CIGS Solar Module With an Efficiency of 17.9%," AVANCIS 2016, accessed September 16, 2022, <https://www.avancis.de/en/module-with-record-efficiency-from-avancis/>.
8. D. Hauschild, F. Meyer, A. Benkert, et al., "Annealing-Induced Effects on the Chemical Structure of the In₂S₃/CuIn(S,Se)₂ Thin-Film Solar Cell Interface," *Journal of Physical Chemistry C* 119, no. 19 (2015): 10412–10416, <https://doi.org/10.1021/acs.jpcc.5b01622>.
9. D. Hauschild, F. Meyer, A. Benkert, et al., "Improving Performance by Na Doping of a Buffer Layer—Chemical and Electronic Structure of the In_xS_y:Na/CuIn(S,Se)₂ Thin-Film Solar Cell Interface," *Progress in Photovoltaics* 26, no. 5 (2018): 359–366, <https://doi.org/10.1002/pip.2993>.
10. S. Spiering, A. Nowitzki, F. Kessler, M. Igalson, and H. Abdel Maksoud, "Optimization of Buffer-Window Layer System for CIGS Thin Film Devices With Indium Sulphide Buffer by In-Line Evaporation," *Solar Energy Materials and Solar Cells* 144 (2016): 544–550, <https://doi.org/10.1016/j.solmat.2015.09.038>.
11. Q. Nguyen, K. Orgassa, I. Koetschau, U. Rau, and H. W. Schock, "Influence of Heterointerfaces on the Performance of Cu(In,Ga)Se₂ Solar Cells With CdS and In(OH_xS_y) Buffer Layers," *Thin Solid Films* 431–432 (2003): 330–334, [https://doi.org/10.1016/S0040-6090\(03\)00156-1](https://doi.org/10.1016/S0040-6090(03)00156-1).
12. A. Strohm, L. Eisenmann, R. K. Gebhardt, et al., "ZnO/In_xS_y/Cu(In,Ga)Se₂ Solar Cells Fabricated by Coherent Heterojunction Formation," *Thin Solid Films* 480–481 (2005): 162–167, <https://doi.org/10.1016/j.tsf.2004.11.032>.
13. U. Rau and M. Schmidt, "Electronic Properties of ZnO/CdS/Cu(In,Ga)Se₂ Solar Cells — Aspects of Heterojunction Formation," *Thin Solid Films* 387, no. 1 (2001): 141–146, [https://doi.org/10.1016/S0040-6090\(00\)01737-5](https://doi.org/10.1016/S0040-6090(00)01737-5).
14. A. H. Jahagirdar, A. A. Kadam, and N. G. Dhere, "Role of i-ZnO in Optimizing Open Circuit Voltage of CIGS₂ and CIGS Thin Film Solar Cells," in *2006 IEEE 4th World Conference on Photovoltaic Energy Conference* (2006), 557–559. <https://doi.org/10.1109/WCPEC.2006.279516>.
15. S. Ishizuka, K. Sakurai, A. Yamada, et al., "Fabrication of Wide-Gap Cu(In_{1-x}Ga_x)Se₂ Thin Film Solar Cells: A Study on the Correlation of Cell Performance With Highly Resistive i-ZnO Layer Thickness," *Solar Energy Materials & Solar Cells* 87, no. 1 (2005): 541–548, <https://doi.org/10.1016/j.solmat.2004.08.017>.
16. S. Alhammedi, H. Park, and W. K. Kim, "Optimization of Intrinsic ZnO Thickness in Cu(In,Ga)Se₂-Based Thin Film Solar Cells," *Materials* 12, no. 9 (2019): 1365, <https://doi.org/10.3390/ma12091365>.
17. R. Scheer, L. Messmann-Vera, R. Klenk, and H.-W. Schock, "On the Role of Non-doped ZnO in CIGSe Solar Cells," *Progress in Photovoltaics: Research and Applications* 20, no. 6 (2012): 619–624, <https://doi.org/10.1002/pip.1185>.
18. L. Weinhardt, C. Heske, E. Umbach, T. P. Niesen, S. Visbeck, and F. Karg, "Band Alignment at the i-ZnO/CdS Interface in Cu(In,Ga)(S,Se)₂ Thin-Film Solar Cells," *Applied Physics Letters* 84, no. 16 (2004): 3175–3177, <https://doi.org/10.1063/1.1704877>.
19. Y. Abe, A. Komatsu, H. Nohira, et al., "Interfacial Layer Formation at ZnO/CdS Interface," *Applied Surface Science* 258, no. 20 (2012): 8090–8093, <https://doi.org/10.1016/j.apsusc.2012.04.177>.
20. L. Weinhardt, "Elektronische und chemische Eigenschaften von Grenzflächen und Oberflächen in optimierten Cu(In,Ga)(S,Se)₂ Dünnschichtszellzellen" (Dissertation, University of Würzburg, 2005).
21. J. F. Moulder, W. F. Stickle, P. E. Sobol, and K. D. Bomben, *Handbook of X-Ray Photoelectron Spectroscopy* (Physical Electronics Division, Perkin-Elmer Corporation, 1992).
22. M. Blum, L. Weinhardt, O. Fuchs, et al., "Solid and Liquid Spectroscopic Analysis (SALSA)—A Soft X-Ray Spectroscopy Endstation With a Novel Flow-Through Liquid Cell," *Review of Scientific Instruments* 80, no. 12 (2009): 123102, <https://doi.org/10.1063/1.3257926>.
23. O. Fuchs, L. Weinhardt, M. Blum, et al., "High-Resolution, High-Transmission Soft X-Ray Spectrometer for the Study of Biological Samples," *Review of Scientific Instruments* 80, no. 6 (2009): 063103, <https://doi.org/10.1063/1.3133704>.
24. L. Weinhardt, D. Hauschild, R. Steininger, et al., "Sulfate Speciation Analysis Using Soft X-Ray Emission Spectroscopy," *Analytical Chemistry* 93, no. 23 (2021): 8300–8308, <https://doi.org/10.1021/acs.analchem.1c01187>.
25. C. Heske, R. Fink, E. Umbach, W. Riedl, and F. Karg, "Na-Induced Effects on the Electronic Structure and Composition of Cu(In,Ga)Se₂ Thin-Film Surfaces," *Applied Physics Letters* 68, no. 24 (1996): 3431–3433, <https://doi.org/10.1063/1.115783>.
26. C. Heske, G. Richter, Z. Chen, et al., "Influence of Na and H₂O on the Surface Properties of Cu(In,Ga)Se₂ Thin Films," *Journal of Applied Physics* 82, no. 5 (1997): 2411, <https://doi.org/10.1063/1.366096>.
27. C. Heske, D. Eich, R. Fink, et al., "Localization of Na Impurities at the Buried CdS/Cu(In,Ga)Se₂ Heterojunction," *Applied Physics Letters* 75, no. 14 (1999): 2082–2084, <https://doi.org/10.1063/1.124923>.
28. D. Braunger, D. Hariskos, G. Bilger, U. Rau, and H. W. Schock, "Influence of Sodium on the Growth of Polycrystalline Cu(In,Ga)Se₂ Thin Films," *Thin Solid Films* 361–362 (2000): 161–166, [https://doi.org/10.1016/S0040-6090\(99\)00777-4](https://doi.org/10.1016/S0040-6090(99)00777-4).
29. D. Hauschild, F. Meyer, S. Pohlner, et al., "Impact of Environmental Conditions on the Chemical Surface Properties of Cu(In,Ga)(S,Se)₂ Thin-Film Solar Cell Absorbers," *Journal of Applied Physics* 115, no. 18 (2014): 183707, <https://doi.org/10.1063/1.4876257>.
30. F. Erfurth, B. Hußmann, A. Schöll, et al., "Chemical Structure of the (Zn_{1-x}Mg_x)O/CuIn(S,Se)₂ Interface in Thin Film Solar Cells," *Applied Physics Letters* 95, no. 12 (2009): 122104, <https://doi.org/10.1063/1.3230071>.
31. A. Naumkin, A. Kraut-Vass, S. Gaarenstroom, and C. Powell, "NIST X-Ray Photoelectron Spectroscopy (XPS) Database, Version 5.0," accessed November 30, 2023, <https://dx.doi.org/10.18434/T4T88K>.
32. D. Kreikemeyer-Lorenzo, D. Hauschild, P. Jackson, et al., "Rubidium Fluoride Post-Deposition Treatment: Impact on the Chemical Structure of the Cu(In,Ga)Se₂ Surface and CdS/Cu(In,Ga)Se₂ Interface in Thin-Film Solar Cells," *ACS Applied Materials & Interfaces* 10, no. 43 (2018): 37602, <https://doi.org/10.1021/acsami.8b10005>.
33. V. R. van Maris, D. Hauschild, T. P. Niesen, et al., "Impact of UV-Induced Ozone and Low-Energy Ar⁺-Ion Cleaning on the Chemical Structure of Cu(In,Ga)(S,Se)₂ Absorber Surfaces," *Journal of Applied Physics* 128, no. 15 (2020): 155301, <https://doi.org/10.1063/5.0020253>.
34. C. D. Wagner and A. Joshi, "The Auger Parameter, Its Utility and Advantages: A Review," *Journal of Electron Spectroscopy and Related Phenomena* 47 (1988): 283–313, [https://doi.org/10.1016/0368-2048\(88\)85018-7](https://doi.org/10.1016/0368-2048(88)85018-7).
35. W. Kogler, T. Schnabel, E. Ahlswede, et al., "Hybrid Chemical Bath Deposition-CdS/Sputter-Zn(O,S) Alternative Buffer for Cu₂ZnSn(S,Se)₄ Based Solar Cells," *Journal of Applied Physics* 127, no. 16 (2020): 165301, <https://doi.org/10.1063/1.5142550>.

36. K. Horsley, R. J. Beal, R. G. Wilks, et al., "Impact of Annealing on the Chemical Structure and Morphology of the Thin-Film CdTe/ZnO Interface," *Journal of Applied Physics* 116, no. 2 (2014): 024312, <https://doi.org/10.1063/1.4890235>.
37. G. Deroubaix and P. Marcus, "X-Ray Photoelectron Spectroscopy Analysis of Copper and Zinc Oxides and Sulphides," *Surface and Interface Analysis* 18, no. 1 (1992): 39–46, <https://doi.org/10.1002/sia.740180107>.
38. D. Hauschild, M. Blankenship, A. Hua, et al., "Chemical and Electronic Structure at the Interface Between a Sputter-Deposited Zn(O,S) Buffer and a Cu(In,Ga)(S,Se)₂ Solar Cell Absorber," *Solar RRL* 7 (2023): 2201091, <https://doi.org/10.1002/solr.202201091>.
39. S. W. Gaarenstroom and N. Winograd, "Initial and Final State Effects in the ESCA Spectra of Cadmium and Silver Oxides," *Journal of Chemical Physics* 67, no. 8 (1977): 3500–3506, <https://doi.org/10.1063/1.435347>.
40. M. Bär, J. Reichardt, A. Grimm, et al., "Zn(O,OH) Layers in Chalcopyrite Thin-Film Solar Cells: Valence-Band Maximum Versus Composition," *Journal of Applied Physics* 98, no. 5 (2005): 053702, <https://doi.org/10.1063/1.2034650>.
41. J.-C. Dupin, D. Gonbeau, P. Vinatier, and A. Levasseur, "Systematic XPS Studies of Metal Oxides, Hydroxides and Peroxides," *Physical Chemistry Chemical Physics* 2, no. 6 (2000): 1319–1324, <https://doi.org/10.1039/A908800H>.
42. J. Duchoslav, R. Steinberger, M. Arndt, and D. Stifter, "XPS Study of Zinc Hydroxide as a Potential Corrosion Product of Zinc: Rapid X-Ray Induced Conversion Into Zinc Oxide," *Corrosion Science* 82 (2014): 356–361, <https://doi.org/10.1016/j.corsci.2014.01.037>.
43. M. Mezher, R. Garris, L. M. Mansfield, et al., "Soft X-Ray Spectroscopy of a Complex Heterojunction in High-Efficiency Thin-Film Photovoltaics: Intermixing and Zn Speciation at the Zn(O,S)/Cu(In,Ga)Se₂ Interface," *ACS Applied Materials & Interfaces* 8, no. 48 (2016): 33256–33263, <https://doi.org/10.1021/acsami.6b09245>.
44. M. Bär, N. Barreau, F. Couzinié-Devy, et al., "Nondestructive Depth-Resolved Spectroscopic Investigation of the Heavily Intermixed In₂S₃/Cu(In,Ga)Se₂ Interface," *Applied Physics Letters* 96, no. 18 (2010): 184101, <https://doi.org/10.1063/1.3425739>.
45. C. Heske, U. Groh, O. Fuchs, et al., "X-Ray Emission Spectroscopy of Cu(In,Ga)(S,Se)₂-Based Thin Film Solar Cells: Electronic Structure, Surface Oxidation, and Buried Interfaces," *Physica Status Solidi* 187, no. 1 (2001): 13–24, [https://doi.org/10.1002/1521-396X\(200109\)187:1<13::AID-PSSA13>3.0.CO;2-D](https://doi.org/10.1002/1521-396X(200109)187:1<13::AID-PSSA13>3.0.CO;2-D).
46. C. Heske, U. Groh, O. Fuchs, et al., "Monitoring Chemical Reactions at a Liquid–Solid Interface: Water on CuIn(S,Se)₂ Thin Film Solar Cell Absorbers," *Journal of Chemical Physics* 119, no. 20 (2003): 10467, <https://doi.org/10.1063/1.1627328>.
47. A. Meisel, G. Leonhardt, and R. Szargan, "Röntgenspektren und Chemische Bindung," (Leipzig Geest & Portig, 1977).
48. L. Weinhardt, D. Hauschild, and C. Heske, "Surface and Interface Properties in Thin-Film Solar Cells: Using Soft X-Rays and Electrons to Unravel the Electronic and Chemical Structure," *Advanced Materials* 31, no. 26 (2019): 1806660, <https://doi.org/10.1002/adma.201806660>.
49. T. Gleim, C. Heske, E. Umbach, et al., "Formation of the ZnSe/(Te/) GaAs(100) Heterojunction," *Surface Science* 531, no. 1 (2003): 77–85, [https://doi.org/10.1016/S0039-6028\(03\)00439-4](https://doi.org/10.1016/S0039-6028(03)00439-4).
50. T. Gleim, C. Heske, E. Umbach, et al., "Reduction of the ZnSe/GaAs(100) Valence Band Offset by a Te Interlayer," *Applied Physics Letters* 78, no. 13 (2001): 1867–1869, <https://doi.org/10.1063/1.1358366>.
51. V. Srikant and D. R. Clarke, "On the Optical Band Gap of Zinc Oxide," *Journal of Applied Physics* 83, no. 10 (1998): 5447–5451, <https://doi.org/10.1063/1.367375>.
52. B. E. Sernelius, K.-F. Berggren, Z.-C. Jin, I. Hamberg, and C. G. Granqvist, "Band-Gap Tailoring of ZnO by Means of Heavy Al Doping," *Physical Review B* 37, no. 17 (1988): 10244–10248, <https://doi.org/10.1103/PhysRevB.37.10244>.
53. F. Erfurth, A. Grimm, J. Palm, et al., "Direct Determination of the Band Alignment at the (Zn,Mg)O/CISSe Interface," *Applied Physics Letters* 98, no. 14 (2011): 142107, <https://doi.org/10.1063/1.3565972>.
54. M. Wang, L. Jiang, E. J. Kim, and S. H. Hahn, "Electronic Structure and Optical Properties of Zn(OH)₂: LDA+U Calculations and Intense Yellow Luminescence," *RSC Advances* 5, no. 106 (2015): 87496–87503, <https://doi.org/10.1039/C5RA17024A>.
55. D. A. Duncan, R. Mendelsberg, M. Mezher, et al., "A New Look at the Electronic Structure of Transparent Conductive Oxides—A Case Study of the Interface Between Zinc Magnesium Oxide and Cadmium Telluride," *Advanced Materials Interfaces* 3, no. 22 (2016): 1600418, <https://doi.org/10.1002/admi.201600418>.